CEAS Space Journal
https://doi.org/10.1007/s12567-026-00775-3

ORIGINAL PAPER

Fluid–structure-coupled simulations of heat transfer in hybrid rocket engine nozzles

Jan Erik Zeriadtke[1] · **Sebastian Jack**[1] · **Viola Wartemann**[1]

Received: 15 April 2026 / Revised: 29 June 2026 / Accepted: 1 October 2026
© The Author(s) 2026

Abstract
In hybrid rocket engines, the nozzle experiences high temperatures that can lead to erosion, especially when passively cooled designs are used. The temperature at the fluid–structure interface plays a critical role in nozzle erosion, and understanding the heat transfer at this interface is essential for accurate erosion modelling. This study presents high- and low-fidelity coupled simulations of nozzle heating, combining computational fluid dynamics (CFD) and computational solid mechanics (CSM) to analyse transient heat transfer in hybrid rocket engine nozzles. In the high-fidelity case, axisymmetric simulations are performed. The reactive flow in the nozzle is simulated using the DLR TAU code, with RANS simulations and a chemical non-equilibrium model to capture the fluid flow. The thermal response of the nozzle structure is calculated using finite element analysis with Ansys, modelling the two-dimensional heating of the nozzle material. These two domains, computational fluid dynamics (CFD) and computational solid mechanics (CSM), are coupled using the DLR coupled numerical fluid, flight mechanics and structure simulations ($CoNF^2aS^2$) tool, which facilitates the exchange of heat flux and temperature data between the fluid and structure simulations. The high-fidelity simulation results are compared with pre-design calculations. These low-fidelity calculations use thermodynamic relationships and semi-empirical methods to estimate the heat flux at the fluid–structure interface, and one-dimensional heat conduction in the structure to model the temperature response. The simulations are applied to the nozzle geometry of the AHRES-C hybrid rocket engine with a graphite insert. The low-fidelity simulations are validated by comparing their results with high-fidelity predictions, thereby providing an evaluation of the accuracy of pre-design methods. The methods show good agreement in the converging and throat nozzle sections in terms of heat flux and temperatures. This makes the low-fidelity method a good design tool for the sizing of thermal protection. In the diverging nozzle section, the low-fidelity approach underpredicts the heat fluxes and temperatures, as it cannot account for the formation of an oblique shock. This analysis enhances the understanding of heat transfer in hybrid rocket engine nozzles, further informing design decisions and optimization strategies.

Keywords Hybrid rocket engine · CFD · Fluid–stucture-interaction · $CoNF^2aS^2$ · Heat transfer · Rocket nozzle

1 Introduction

Hybrid rocket engines (HREs) represent a promising alternative to conventional solid and liquid rocket engines. These engines are a combination of both concepts, typically employing a liquid or gaseous oxidizer and a solid fuel. The combination of intrinsic safety with favourable performance parameters, in addition to the possibility of throttling, renders them a valuable research platform. The Spacecraft department of the German Aerospace Center (DLR) Institute of Aerodynamics and Flow Technology (AS) is developing the preliminary design software Advanced Hybrid Rocket Engine Simulation (AHRES) for the fast and reliable design of hybrid and solid rocket engines. The software uses semi-empirical methods, which are verified by numerical and experimental investigations [1]. For numerical comparisons, two- and three-dimensional simulations are performed by the DLR are performed by the DLR TAU-Code [2]. These CFD

✉ Jan Erik Zeriadtke
Jan.Zeriadtke@dlr.de

Sebastian Jack
Sebastian.Jack@dlr.de

Viola Wartemann
Viola.Wartemann@dlr.de

[1] Institute of Aerodynamics and Flow Technology, Department Spacecraft, German Aerospace Center (DLR e.V.), Lilienthalplatz 7, 38108 Braunschweig, Germany

Published online: 28 October 2026

simulations include a detailed combustion process for hydrogen peroxide (H_2O_2) and hydroxyl-terminated polybutadien (HTPB) [3–7].

The erosion of the nozzle remains a significant challenge in HREs [8]. Therefore, the scope of AHRES was expanded to encompass the simulation of graphite nozzle insert erosion. These simulations, which are based on semi-empirical heat transfer simulations, showed some differences in the erosion profile when compared to experimental data [9]. From this, the opportunity was taken to evaluate the accuracy of the heat transfer modelling.

A limited number of available studies evaluate the heat transfer in HRE nozzles experimentally. Narsai et al. [10] measured temperatures in the throat plane over a short burn duration and calculated the heat flux. Comparison with the Bartz equation showed good agreement, but this was only evaluated at the throat plane and only for the cold wall case. Kamps et al. [11] reconstructed the wall temperature in the nozzle throat from measured temperatures in the nozzle material and one-dimensional heat conduction modelling.

Multiple numerical studies have focused on nozzle erosion and calculated the heat transfer with fluid–structure-coupled methods.

Bianchi and Nasuti [12] studied the chemical nozzle erosion. The heat transfer is calculated by solving the Reynolds-averaged Navier–Stokes (RANS) equations on the fluid side. An erosion model based on the heat of ablation and a steady-state, adiabatic temperature distribution is used in the solid.

Zhao et al. [13] and Tian et al. [14] calculated the nozzle erosion based on steady-state computations. The stationary flow and temperature fields are calculated from CFD and one-dimensional heat equation normal to the surface.

Tian et al. [15] simulated transient nozzle erosion. For this, the time-resolved flow field is calculated with a moving mesh model to capture nozzle wall erosion. In the structure, one-dimensional heat conduction normal to the surface is considered.

Zhang et al. [16] set up a coupled CFD–CSM scheme to simulate nozzle erosion. They used a loose, two-way coupling between transient flow field and structure heating. Additionally, they one-way coupled the steady-state mechanical and chemical erosion rates to realize the mesh movement due to erosion inside the transient simulation.

Rotondi et al. [17] utilized empirical, closed-form nozzle regression laws to determine transient erosion rates and wall temperatures from experimental data. These were then one-way coupled as transient boundary conditions to a one-dimensional heating solver, calculating the thermal response of the nozzle structure. The calculated temperature profiles in the throat were then compared to data from experiments with embedded thermocouples.

In the field of solid rocket motors, multiple studies deal with heat transfer in different passively cooled nozzles. Cross and Boyd [18] set up a coupling of steady-state fluid simulations with a two-dimensional, transient material response solver to investigate the ablation of pyrolyzing materials. They compared different formulations of surface energy balances. This was later expanded to finite-rate chemistry for pyrolysis [19].

Hao et al. [20] considered the influence of alumina particles by investigating the effects of two-phase flow and radiative heat transfer in solid rocket motor nozzles. They found significant effects on heat flux, wall temperature, and erosion rate from the particles.

In liquid rocket engines, most studies focus on steady-state heat transfer, as the chamber and nozzle walls are generally cooled regeneratively. Hötte and Haupt [21] investigated the heating of a cooled combustion chamber by transient coupling of hot fluid, structure, and coolant flow.

Shin et al. [22] compared different semi-empirical heat transfer equations to a CFD from Betti [23] for a regeneratively cooled methane/oxygen rocket engine at steady state.

Potier et al. [24] performed a conjugated heat transfer simulation by coupling a large-eddy simulation to a conduction solver to predict steady-state heat fluxes in a hydrogen/oxygen rocket engine.

Concio et al. [25] investigated the heat flux of a regeneratively cooled methane/oxygen rocket engine with prescribed wall temperatures from experimental data.

To validate the previously employed low-fidelity heat transfer model, high-fidelity simulations were performed. In this work, the comparison is carried out between the semi-empirical approach and a high-fidelity predictor–corrector coupling between CFD and CSM.

2 Methods

This chapter introduces the nozzle geometry that defines the computational domain for all simulations. It then details the low-fidelity semi-empirical heat transfer model and the high-fidelity predictor–corrector CFD–CSM coupling.

2.1 Engine geometry

The chosen geometry for this study is the nozzle assembly of the AHRES-C hybrid rocket engine, see Fig. 1. The engine utilizes HTPB as a fuel and H_2O_2 as an oxidizer, which is decomposed in a novel catalytic chamber, featuring two oxidizer injection paths [26]. This enables the possibility of advanced throttling concepts [27]. The design parameters of the engine are a maximum oxidizer mass flow of 1 kg/s, a chamber pressure of $p_c = 5$MPa, and a burntime of 30s. From this, a nozzle throat diameter of $d_t = 20.8$ mm is chosen. To

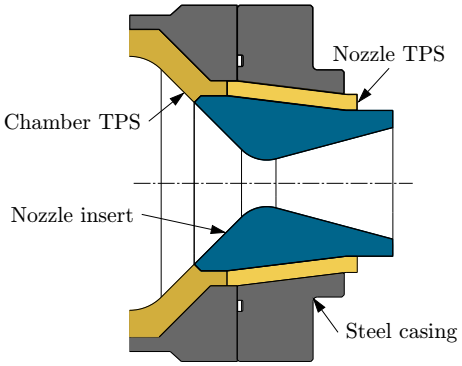


Fig. 1 Nozzle assembly of the AHRES-C engine

enable a deep throttling range without flow separation in the nozzle, a low expansion ratio of 5.78 is chosen, leading to an exit diameter of 50mm. For the nozzle contour, a typical laval profile with half-angles of 45° and 15° in the converging and diverging sections, and a throat curvature radius of $R_{\text{curv}} = 16\,\text{mm}$ are used.

The nozzle structure consists of multiple parts, as shown in Fig. 1. Upstream, the post-combustion chamber thermal protection system (TPS) is made from carbon fibre phenolic composite, and provides the first converging section. Then the main nozzle contour, including the throat and diverging section, is designed as a single nozzle insert, made here from graphite. To thermally insulate the graphite insert, a nozzle TPS part, made of phenolic paper, is used. Both the nozzle insert and nozzle TPS feature a conical outer profile of 7° to transfer the pressure loads of the engine chamber to the casing and provide sealing without dedicated sealing materials. The outer engine casing is made of high-temperature stainless steel to carry mechanical loads. The material properties used for the thermal structure simulations are listed in Table 1. As the engine casing should not experience any heating during the burntime, it is excluded from the simulations.

2.2 Low-fidelity simulations

For pre-design calculations, a method based on semi-empirical heat transfer correlations and one-dimensional radial heat conduction is used. To calculate the convective heat transfer coefficient h between the fluid and the nozzle structure, the Bartz equation [28] is used:

$$h = \left[\frac{0.026}{d_t^{0.2}} \frac{\mu_c^{0.2} C_{p,c}}{Pr_c^{0.6}} \left(\frac{p_c}{c^*}\right)^{0.8} \left(\frac{d_t}{R_{\text{curv}}}\right)^{0.1}\right] \left(\frac{A_t}{A(x)}\right)^{0.9} \sigma. \tag{1}$$

Here, μ_c, $C_{p,c}$, Pr_c and p_c are the viscosity, heat capacity, Prandtl number, and pressure of the fluid, each evaluated inside the combustion chamber, as denoted by index c. The characteristic velocity of the engine is c^*. The area at the throat is denoted A_t and the area at each position along the nozzle $A(x)$.

The other variable properties are expressed as

$$\sigma = \left[\frac{1}{2}\left(\frac{T_w}{T_c}\right)\left(1 + \frac{\gamma - 1}{2} M^2\right) + \frac{1}{2}\right]^{-0.68} \cdot \left[1 + \frac{\gamma - 1}{2} M^2\right]^{-0.12}. \tag{2}$$

The local temperature at the wall is T_w and the stagnation temperature in the chamber T_c. The Mach number M and the heat capacity ratio γ are also evaluated at each area ratio $\frac{A(x)}{A_t}$. Additionally, the pressure $p(x)$ and the fluid temperature $T(x)$ are calculated for each area ratio. The Eqs. (1) and (2) represent a closed-form solution of the turbulent boundary layer flow where the leading factor of 0.026 was determined by empirical fitting [29].

All needed thermodynamic properties are calculated with the Chemical Equilibrium with Applications (CEA) code [30, 31] via the python interface RocketCEA [32]. These CEA calculations assume a frozen flow inside the nozzle and a chamber pressure of 5MPa. The propellants are 87.5% H_2O_2 and HTPB, the latter modelled as $C_{7.3165}H_{10.3360}O_{0.1063}$, with an enthalpy of formation of 5024.16kJ/kg [32]. A constant oxidizer–fuel ratio of 6.8 was chosen, near the optimum of characteristic velocity for that propellant combination [33].

The calculated heat transfer coefficient can then be used as the boundary condition for the one-dimensional transient heat conduction in the solid. In radial coordinates, the heat equation in a non-uniform medium is

$$C_p \rho \frac{\partial T}{\partial t} = \frac{1}{R} \frac{\partial}{\partial R}\left(Rk \frac{\partial T}{\partial R}\right). \tag{3}$$

The convective inner boundary condition is expressed as

$$k \frac{\partial T}{\partial R} - h\,(T_w - T(x)) = 0. \tag{4}$$

For the outer boundary conditions, adiabatic boundaries are assumed. A uniform discretization with central differences is used in the radial direction and an implicit Crank–Nicolson scheme in time. The temperature dependent material properties are updated after every timestep from the calculated temperature profile (lagging of coefficients) [34].

Table 1 lists the material properties C_p, k, and ρ which are the heat capacity, thermal conductivity, and density of the nozzle materials.

Transient calculation is then performed by solving Eq. 3 towards the next timestep, resulting in a new wall temperature. From this, the heat transfer coefficient is updated for

Table 1 Material properties for heat conduction

	Nozzle insert	Chamber TPS	Nozzle TPS
Material	Graphite	Carbon fibre phenolic composite	Phenolic paper
ρ $(\mathrm{kg/m^3})$	1840	1460	1350
k (W/m K)	$3712 \cdot T^{-0.6}$ [11]	0.134	0.25
C_p (J/kg K)	$651 \cdot \log(T) - 2877$ [11]	1130	1260

the next timestep. This represents a loose coupling approach between the convective heat transfer and the heat conduction without an inner predictor–corrector loop. Together, this is a completely local method, where each position along the nozzle can be calculated independently of every other position. For the results presented, 150 slices in axial direction, each with 150 steps in radial direction, are computed.

2.3 High-fidelity simulations

High-fidelity simulations based on axisymmetric RANS and finite element method (FEM) simulations are performed. These single field solutions are coupled with the Coupled Numerical Fluid, Flightmechanics and Structure Simulations ($\mathrm{CoNF^2aS^2}$) tool. The time-accurate heating of the structure is calculated by the CSM solver Ansys. For the fluid domain, the DLR TAU-Code is used.

2.3.1 Numerical setup

The Reynolds-averaged Navier–Stokes (RANS) equations are solved with the DLR TAU-Code. This code has been extensively validated for modelling rocket propulsion systems [35] and is able to predict heat fluxes and wall temperatures in combustion chambers and nozzles [36, 37].

For turbulence modelling, the single equation Spalart-Allmaras (SA) model in the negative formulation [38] is used. The flow domain is set up as a two-dimensional, axisymmetric case. For inflow conditions, the equilibrium chamber values from CEA calculations are taken as a uniform mass flux inlet. The inflow species mass fractions are listed in Table 2, and the inflow temperature is set to $T_c = 2843\mathrm{K}$. The total mass flow rate is adjusted to 1.06kg/s to reach the design chamber pressure of 5MPa at the inflow boundary. A supersonic outflow condition is used at the nozzle exit to achieve stable flow conditions. All walls are treated as viscous walls. The wall of the post-combustion-chamber is assumed to be adiabatic. The wall of the nozzle insert is used as the interface for the fluid–structure-interaction. For the initial solution, a wall temperature of 293.15K is assumed. For better numerical stability, this is accomplished by a thermal-reservoir boundary condition.

The Westbrook and Dryer finite rate reaction mechanism [39] is further simplified for the nozzle flow. As equilibrium conditions are used as inflow, no C_4H_6 is expected to be present and can be removed from the mechanism. Therefore, a version with 11 species and a total of 20 reactions is used.

Convergence of the iterations is determined by a Cauchy criterion of the total heat flow. This stops the fluid iterations as soon as the heat flow changes less than 0.05% over the last 5% of iterations.

For the CSM domain the solver Ansys Mechanical 2022R2 is used. The simulation is set up as transient thermal, where the coupled interface applies a heat flux. The outer boundaries are set as adiabatic everywhere, identical to the low-fidelity case. A three-dimensional simulation with one element in circumferential direction is performed, making the simulation quasi-axisymmetric. The mesh contains 10319 quadratic order elements of type *SOLID279*, of which 6308 are in the insert part. Internal contacts between the parts are implemented with *CONTA174* elements, but neglecting any thermal contact resistance. Material properties are taken from Table 1, identical to the low-fidelity simulation.

2.3.2 Coupling scheme

Figure 2 shows a schematic overview of the coupling procedure that was applied to proceed from time step t_i to t_{i+1}. In a first step, the CFD solver computes the aerothermal loads (i.e. surface heat flux) which are interpolated onto the structural domain (1). The CSM solver uses these as boundary conditions and computes the actual surface temperature data (2, predictor step) which are interpolated to the fluid domain (3) and set as boundary conditions in the latter. The CFD solver then proceeds to time step t_{i+1} (4) and returns the updated loads to the CSM domain at the preceding time step (5). Based on this updated information, at least one corrector loop (dashed lines, analogue to 2, 3, 4) is calculated. The difference of the norm of the boundary condition data of two consecutive inner loops is used as convergence criterion. For the presented results, up to seven corrector loops were performed to reach a normalized residual of 10^{-3} for each time step. All CFD results (4) were obtained using steady-state simulations to improve performance and numerical stabil-

Table 2 Inflow species mass fractions from CEA

H_2O	CO_2	CO	OH	O_2	H_2	O	H	HO_2	H_2O_2
0.601	0.321	0.0586	9.97×10^{-3}	6.14×10^{-3}	2.80×10^{-3}	3.20×10^{-4}	8×10^{-5}	2×10^{-5}	1×10^{-5}

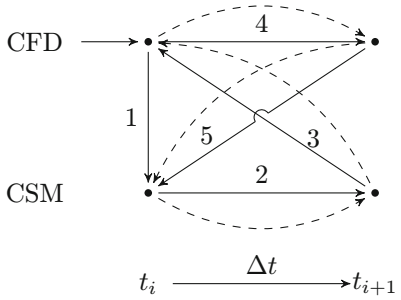


Fig. 2 Partitioned domain solver coupling scheme [40]

Table 3 Mesh parameters and results of fluid grid convergence study

	Coarse (3)	Medium (2)	Fine (1)
Cells	7763	15,996	32,973
Points	6450	13,077	26,282
Quadrilateral layers	32	45	63
Heat flow (W/deg)	442.99	447.94	450.49
Iterations until Cauchy convergence	249857	295392	359661
GCI (%)	–	1.61	0.84

ity. This assumption of a fluid reacting infinitely fast to a change in boundary conditions is justified by comparison of the largely differing orders of magnitude of typical time scales for the transport processes in the fluid (total residence time in the domain $\mathcal{O}(10^{-4}\,\mathrm{s})$) and structure (duration of heating process $\mathcal{O}(10\mathrm{s})$). The size of the timestep is chosen as $\Delta t = 0.01\mathrm{s}$ for the first 50 coupling steps to resolve the fast initial heating of the cold wall. This is then increased, first to $\Delta t = 0.05\,\mathrm{s}$ until $t = 6\mathrm{s}$ of simulation time and lastly to $\Delta t = 0.1\,\mathrm{s}$ for the remainder.

To enable the coupling procedure between the partitioned domains (here: CFD and CSM domain) the involved solvers have to exchange boundary condition and results data. The FlowSimulator is a software integration framework for high-performance computing (HPC)-ready multidisciplinary simulations, jointly developed by AIRBUS, DLR, and ONERA. It provides functionalities to efficiently exchange all data between the solvers (for more information and application examples see [41, 42]). Instead of the classical approach to define interfaces between all solvers that require data exchange, each solver is integrated into the FlowSimulator as a plugin including a control layer to steer the simulation steps and data interfaces to access boundary condition and solution data.

CoNF^{2}aS^2 builds on top of the FlowSimulator, heavily utilizing its functionality and adding more within its own framework, necessary for spacecraft applications, and is consequently applied here. While the CFD solver TAU provides a native interface to be accessed via the FlowSimulator control layer and exchange data with the FlowSimulator DataManager (FSDM), a similar interface had to be implemented to use Ansys as a FlowSimulator plugin. The interface provides boundary condition data and Ansys Parametric Design Language (APDL) scripts for control over the time stepping procedure that can be processed by Ansys during each solution step. For the import of the mesh and solution data, the interface uses the pyansys module [43]. For data interpolation (1, 3 and 5 in Fig. 2) between the adjacent mesh surfaces of the domains, linear interpolation was used.

The described in-house coupling environment CoNF^{2}aS^2 has been used for multiple spacecraft-related simulations. For an overview, see Wartemann et al. [53], the work by Franze, Barz and others on the aerothermal heating of high-velocity vehicles using models of different fidelity levels [44–46], or those by Reimann and others on aeroelastic effects [47–49].

2.3.3 Convergence study

To evaluate the mesh convergence of the fluid grid, a convergence study with three grids is performed. Here, the case of the initial condition with a wall temperature of $T_w = 293.15\,\mathrm{K}$ is considered. As this is the moment of highest heat fluxes and gradients, this represents a conservative approach over the coupling duration.

A hybrid mesh topology with quadrilateral cells within the boundary layer and triangular cells in the field is used for each simulation. The initial cell height in the boundary layer is held constant at $2 \cdot 10^{-6}$mm until the throat and $4 \cdot 10^{-6}$mm in the conical diverging section. Similarly, the total quad layer height was also held constant to 1mm until the throat and 2mm in the diverging section. This results in a maximum y^+ value of 0.116, low enough to adequately resolve the temperature boundary layer. In the coupled calculations, the maximum y^+ is significantly lower, due to the transient heating of the wall.

An overview of the generated meshes and the results of the convergence study is shown in Table 3. The grid conver-

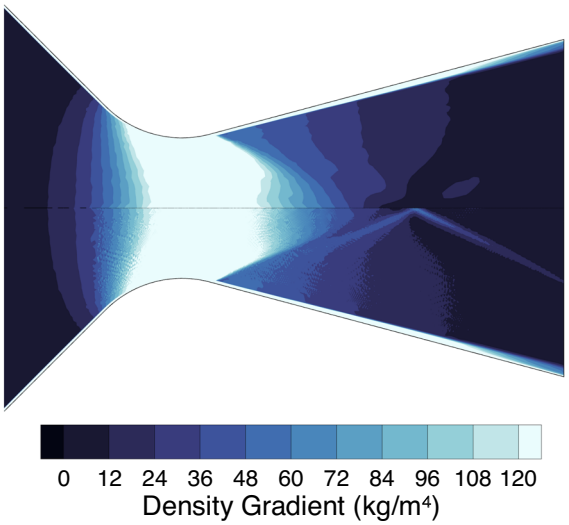


Fig. 3 Density gradient in the fluid field, upper: fine mesh 1, lower: shock-adapted mesh

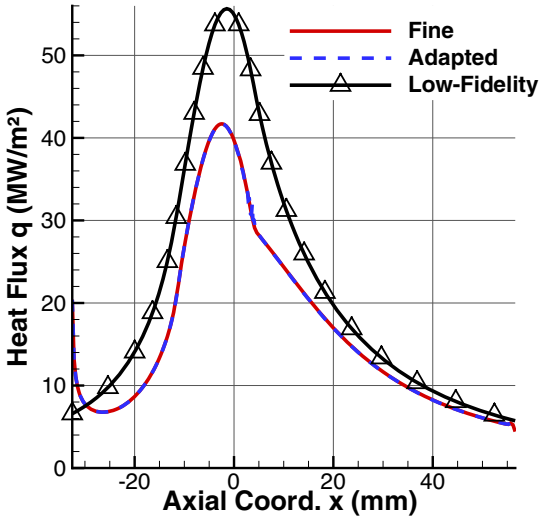


Fig. 4 Cold wall heat flux of the nozzle insert; note, no visible differences between fine and shock-adapted mesh

gence index (GCI) is calculated based on [50, 51]:

$$\mathrm{GCI}_{12} = F_s \cdot \left| \frac{f_2 - f_1}{f_2 \cdot \left(r_{12}^P - 1\right)} \right|. \tag{5}$$

Here, the heat flow over the insert wall is taken as the global quantity f. As three meshes were evaluated for the convergence study, the safety factor was set to $F_s = 1.25$. For the order of convergence for the TAU-Code, $P = 1.75$ is used. The refinement ratio r is calculated from

$$r_{12} = \left(\frac{N_1}{N_2} \right)^{\frac{1}{2}}, \tag{6}$$

based on the number of points N in the two-dimensional grids. This results in an estimated error of $\mathrm{GCI}_{12} < 1\%$ for the finest grid.

Further, the solution was investigated for shocks in the flowfield. In conical nozzles with a circular arc throat, an oblique shock is expected to form at the tangency between the throat curvature and divergent conical section [52]. With the finest grid 1, the main flow field is still too coarse to resolve any shocks, see upper half of Fig. 3. Therefore, this grid was used as a starting point for mesh adaptation based on a shock indicator. The quadrilateral layers were held the same as in the fine mesh 1, while the triangle mesh was refined in 11 steps. This generated a grid with a total of 95 400cells. With this adapted grid, the oblique shocks in the nozzle flow can be seen in the lower half of Fig. 3.

To determine the need to resolve these shocks for the coupled simulations, the cold wall heat fluxes are compared in Fig. 4. Here, the results from the fine mesh 1 and the adapted mesh show no differences. Also, the position of the shock can be seen in the profile of the heat flux as a kink at $x = 4.1$ mm ($x = 0$ is the nozzle throat). As the profile of the heat flux as well as the position of the shock is unaffected by the mesh, the non-adapted fine grid 1 was then used for high-fidelity coupled simulation.

3 Results

Figure 4 shows the cold wall heat fluxes ($t = 0$). Here, x is the axial coordinate with $x = 0$ marking the nozzle throat. For the high-fidelity simulations, the results of the fine mesh as well as a further shock-adapted mesh are shown. As discussed in Sect. 2.3.3, no difference between these simulations is seen. The high-fidelity results show a peak heat flux of $41.7\mathrm{MW/m^2}$ at a position of $x = -2.7$ mm, just upstream of the smallest diameter. At the position of the oblique shock, a kink in the heat flux profile can be seen in the high-fidelity results. Here, the shock raises the heat flux downstream significantly. The peak at the far left of the high-fidelity simulation is due to the change of boundary condition in the fluid simulation at this point. Due to the adiabatic boundary in the post-combustion chamber, the temperature boundary layer is not developed, so the peak in the heat flux at the transition to the coupled interface is expected.

The low-fidelity simulation predicts a significantly higher peak heat flux of $55.6\mathrm{MW/m^2}$. The heat flux also remains higher for the entire nozzle insert, apart from the region at the far left. In the diverging section, both simulations show relatively good agreement. The low-fidelity approach cannot account for shocks reaching into the boundary layer and therefore does not exhibit any kink at the position of the shock.

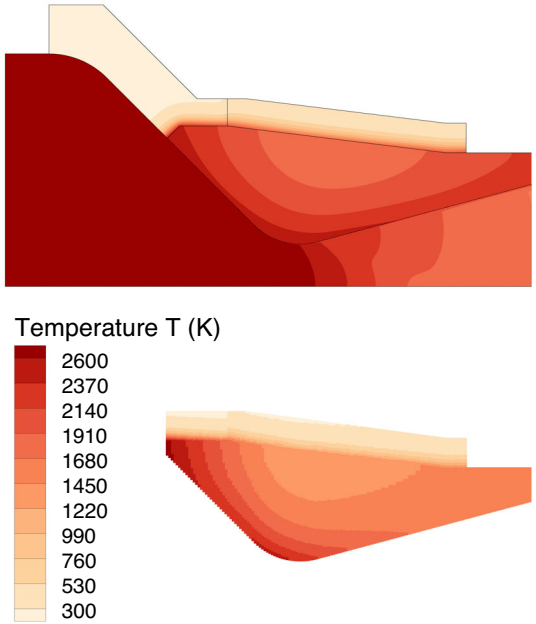


Fig. 5 Temperature fields at $t = 30$s, upper: high fidelity, lower: low fidelity

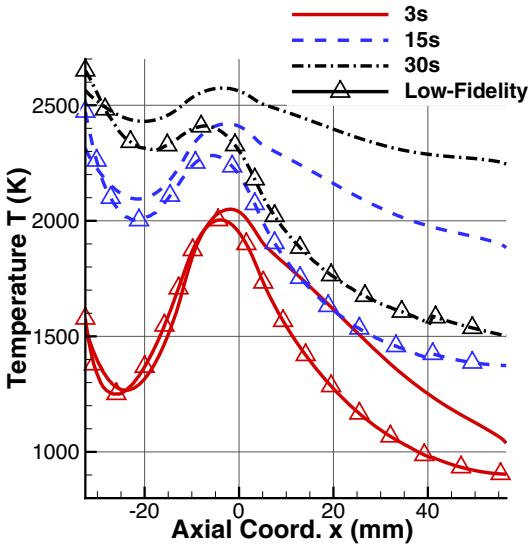


Fig. 6 Wall temperatures of the nozzle at three different times

Figure 5 shows the temperature distributions at $t = 30$s. The fluid and structure result of the high-fidelity simulation is shown on top, and the low-fidelity result below. Qualitatively, there is good agreement between the two simulations. Both show temperature hot spots in the structure just upstream of the throat and at the far left of the nozzle insert. The contour lines show almost concentric circles in the converging section, while the diverging section simulations present major differences. The temperature fields in the TPS materials show steep gradients and remain below 500K in the outer half. Both kinds of TPS show good isolating characteristics, with the carbon fibre-based material of the post-combustion chamber showing slightly better isolation than the phenolic paper, which can be seen at the interface between the two materials in both simulations.

Quantitatively, the high-fidelity simulation shows higher temperatures compared to the low-fidelity case, except for the hot spot at the far left of the nozzle. The low-fidelity simulation reaches a temperature of 2650K at the far left, while the highest temperature of the structure in the high-fidelity case is 2580K at the nozzle throat. In the diverging section downstream of the throat, the high-fidelity results shows higher temperatures by 400K near the throat to 750K at the exit.

Figure 6 shows the wall temperature results of both simulations at three different times. Both simulations show increasing temperatures at every point over time. At $t = 3$s, both methods are closely aligned and show similar temperature profiles in the converging section. The temperature maximum for both methods occurs just upstream of the nozzle throat; here the high-fidelity simulation shows roughly 50K higher temperatures. In the diverging section, the high-fidelity results shows higher temperatures by up to 340K. There, the profile predicted by the high-fidelity simulation drops more linearly, while the low-fidelity case follows a more convex curve.

At $t = 15$s, the low-fidelity simulation predicts the hottest point at the start of the insert with 2440K. At the throat, the simulations start to diverge, with the hottest point of the high-fidelity simulation remaining here and reaching 2420K. Downstream in the diverging section, the high-fidelity result is again hotter, at this time up to 570K.

At the end of the simulated burn time of 30s, the throat temperature of the high-fidelity case reaches 2575K, while the low fidelity case reaches only 2410K. Upstream in the converging section, the low-fidelity result again reaches its peak at now 2650K. The high-fidelity results remains relatively constant, slightly below the throat temperature in this region. Up to the throat, the solutions differ by up to 250K in the converging section. In the diverging nozzle section, the high-fidelity result is significantly hotter, staying above 2250K. The low-fidelity result shows temperatures up to 750K cooler.

Figure 7 shows the calculated heat flux distribution along the nozzle wall, where $x = 0$ is again the nozzle throat. For $t = 3$s, the low-fidelity simulation predicts a peak heat flux of 11.1MW/m^2, 3mm before the smallest diameter. The high-fidelity result reaches a peak of 9.3MW/m^2 at the throat. Due to the oblique shock, the heat flux of the high-fidelity simulation rises again after the throat, reaching its maximum of 9.7MW/m^2 at $x = 10$mm, downstream of the throat. Due to this additional rise in heat flux from the shock, the high-

fidelity result shows significantly higher heat fluxes than the low-fidelity result in the diverging section.

At the later times, the heat fluxes are significantly smaller due to the transient heating of the structure. At $t = 15$s, the peak heat fluxes of the low-fidelity and high-fidelity simulations are 6.2MW/m^2 and 4.7MW/m^2, respectively. For the end of the simulation at $t = 30$s, the low-fidelity method predicts a maximum of 4.25MW/m^2 and the high-fidelity method reaches a maximum of 2.8MW/m^2. The behaviour exhibited by these later time points is similar to the earlier time point and consistent to the wall temperature profile. Again, a significant rise in heat flux can be seen downstream of the throat, which is attributed to the oblique shock. The low-fidelity method cannot account for this shock and therefore underpredicts the heat flux in the diverging section.

To compare heat transfer coefficients shown in Fig. 8, Eq. 1 is used for the low-fidelity results. For the high-fidelity results,

$$\text{h} = \frac{q}{T_{w,\text{ad}} - T_w} \tag{7}$$

is used. The adiabatic wall temperature $T_{w,\text{ad}}$ is taken from an adiabatic CFD-simulation and q is the heat flux from the coupled simulation.

For the cold wall case at $t = 0$s, the low-fidelity calculation predicts a maximum of $24.9\frac{\text{kW}}{\text{m}^2\text{K}}$ at the throat, with the high-fidelity maximum $16.8\frac{\text{kW}}{\text{m}^2\text{K}}$ at 2.5mm upstream of the throat. This high difference is to be expected as the low-fidelity approach has no information on boundary layer history and length [29]. The difference of 48.3% compared to the high-fidelity result also is in the same magnitude as the comparison to CFD by Betti [23] (45%). The profiles along the nozzle follow similar trends as the cold wall heat fluxes in Fig. 4.

At $t = 3$s, the low-fidelity method shows reductions in the heat transfer coefficients along the whole nozzle. The high-fidelity results also show a reduction in h up to the position of the shock. At that position, the heat transfer coefficient rises slightly in downstream direction and remains higher in comparison to the initial time. The maximum for the low-fidelity method reaches $18.4\frac{\text{kW}}{\text{m}^2\text{K}}$, still an overprediction by 43.0% compared to the high-fidelity method with $12.9\frac{\text{kW}}{\text{m}^2\text{K}}$. Over the rest of the simulation time, the heat transfer coefficients of both methods stay almost constant with only minor reductions along the nozzle observable.

In the converging section, the high-fidelity method predicts lower heat fluxes and lower heat transfer coefficients, but higher surface temperatures in comparison to the low-fidelity method. This can be attributed to the one-dimensional modelling of heat conduction in the low-fidelity case. In the high-fidelity case, heat from the throat region can be conducted upstream within the structure, whereas in the low-fidelity case this is not accounted for.

In the diverging section, the high-fidelity method again predicts lower heat transfer coefficients and higher surface temperatures, as well as higher heat fluxes in comparison to the low-fidelity method. This can therefore be traced to a higher driving fluid temperature in the boundary layer due to the shock, compared to the bulk fluid temperature in the low-fidelity method.

Figure 9 shows the temperature profile in radial direction at the throat plane of $x = 0$. In the fluid, up to $y = 10.4$mm, only the high-fidelity results are available as the low-fidelity method does not resolve the fluid temperatures radially. Here, no change of temperature over time can be seen in the core fluid flow.

Moving radially outward, between $y = 10.4$mm and $y = 37$mm, the graphite insert can be seen. Initially at $t = 3$s, the graphite experiences steep temperature gradients despite the good thermal conductivity. Both methods show good agreement and the outer graphite wall experiences only slight heating. At $t = 15$s, the high-fidelity result shows higher temperatures throughout the throat plane, reaching 1250K at the outer edge of the graphite. The low-fidelity method predicts 930K at this point. At the end of the simulations, the graphite shows significantly smaller temperature gradients, as the outer graphite temperature reaches 1760K in the high-fidelity case and 1300K in the low-fidelity result.

Furthest outward, between $y = 37$mm and $y = 45$mm, the nozzle TPS shows steep temperature gradients due to the good insulation properties. Due to the high temperatures at the contact point of the graphite and the composite TPS, decomposition and ablation will take place, further limiting heat flux. In this study, this is not accounted for. Still, the internal temperature does not exceed 500K at the mid-thickness of the material and remains below 310K at the outer boundary in all simulations. Therefore, the TPS-sizing is adequate for the heat load and burn duration.

When comparing the two methods, the resources needed to carry out the simulations should also be taken into account. For the high-fidelity method, approximately 17,900h of CPU time was needed. Due to parallelization of the CFD and CSM solvers, this resulted in a runtime of 186h. Despite the small computational domain and grid-size, this makes the high-fidelity simulation only attainable with dedicated compute-hardware. Although not on the same system, the low-fidelity simulation took 4.25h. As the tool is not yet parallelized, this can be improved in the future. From this difference it can be easily seen, that the high-fidelity coupling approach cannot replace the semi-empirical methods for most calculations in the design phase.

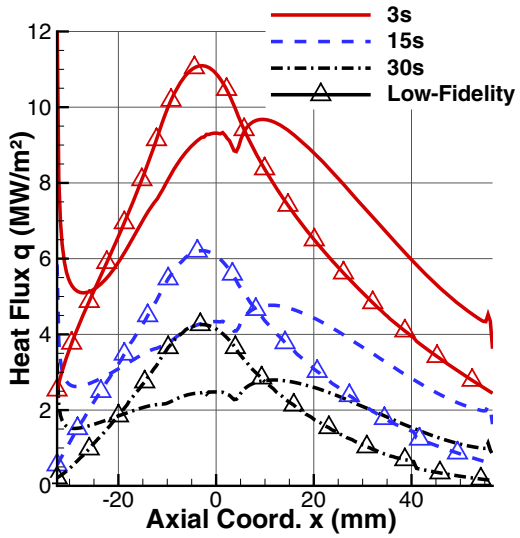


Fig. 7 Heat flux of the nozzle wall at three different times

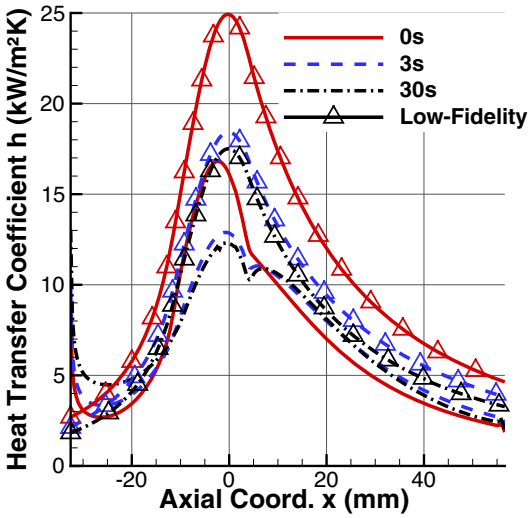


Fig. 8 Heat transfer coefficients at three different times

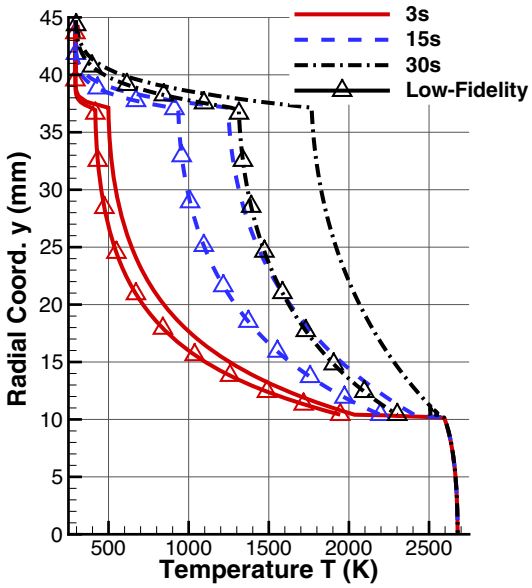


Fig. 9 Radial temperature profiles in the throat plane

4 Conclusion

Simulations of nozzle heat transfer in the AHRES-C hybrid rocket engine were conducted with two different fidelity methods. Both methods show good agreement of the temperatures and heat flux in the converging section and at the nozzle throat. As the throat region experiences the highest heat loads, this validates the low-fidelity approach for the sizing of nozzle TPS.

Due to the oblique shock in the conical nozzle, the heat flux and temperatures in the diverging nozzle section differ substantially. As the low-fidelity method does not account for this shock, its heat fluxes and temperature results are significantly lower. In the converging nozzle region the assumption of one-dimensional heat conduction in the low-fidelity method leads to a smaller underprediction of surface temperatures.

For shock free nozzle contours, a closer agreement is expected and will be verified in the future. Additionally, different empirical heat transfer formulations can be evaluated for the low-fidelity methodology. These could include better approximations for the heat transfer coefficient, as well as corrections for nozzle flows including shocks.

After validating the engine design, experimental static fires of the AHRES-C engine can be utilized to validate not only the low-fidelity approach, but also the high-fidelity method. For this, the engines nozzle assembly will be equipped with thermocouples, measuring the temperatures at different depth inside the nozzle insert.

With the high-fidelity CoNF^{2}aS^2 toolchain established for hybrid rocket nozzle heat transfer, other geometries and variations can be evaluated. Notable here are the bigger VISERION engine, as well as evaluating high-temperature ceramic materials for the nozzle insert, which feature non-isotropic properties.

Acknowledgements The authors gratefully acknowledge the scientific support and HPC resources provided by the German Aerospace Center (DLR). The HPC system CARO is partially funded by "Ministry of Science and Culture of Lower Saxony" and "Federal Ministry of Research, Technology and Space".

Author Contributions Conceptualization: Jan Erik Zeriadtke; methodology: Jan Erik Zeriadtke, Sebastian Jack; formal analysis and investigation: Jan Erik Zeriadtke; writing—original draft preparation: Jan Erik Zeriadtke, Sebastian Jack; writing—review and editing: Jan Erik Zeriadtke, Sebastian Jack, Viola Wartemann; funding acquisition: Viola Wartemann; resources: Viola Wartemann; Supervision: Viola Wartemann.

Funding Open Access funding enabled and organized by Projekt DEAL.

Data availability No datasets were generated or analysed during the current study.

Declarations

Conflict of interest The authors have no relevant financial or non-financial interests to disclose.

Open Access This article is licensed under a Creative Commons Attribution 4.0 International License, which permits use, sharing, adaptation, distribution and reproduction in any medium or format, as long as you give appropriate credit to the original author(s) and the source, provide a link to the Creative Commons licence, and indicate if changes were made. The images or other third party material in this article are included in the article's Creative Commons licence, unless indicated otherwise in a credit line to the material. If material is not included in the article's Creative Commons licence and your intended use is not permitted by statutory regulation or exceeds the permitted use, you will need to obtain permission directly from the copyright holder. To view a copy of this licence, visit http://creativecommons.org/licenses/by/4.0/.

References

1. Božić, O., Porrmann, D., Lancelle, D., Hartwig, A.: Program AHRES and its contribution to assess features and current limitations of hybrid rocket propulsion. In: 63rd International Astronautical Congress, Naples, Italy (2012)
2. Schwamborn, D., Gerhold, T., Heinrich, R.: The DLR TAU-code: recent applications in research and industry. In: ECCOMAS CFD, Netherlands (2006)
3. May, S., Božić, O.: CFD Simulation of chemical non-equilibrium reacting flow within the AHRES hybrid rocket engine. In: 6th European Conference for Aeronautics and Space Sciences, Kraków, Poland (2015)
4. May, S., Božić, O.: Numerical Simulation of the Flow and Combustion Inside the Reaction Chamber of the AHRES Hybrid Rocket Engine. In: Dillmann, A., Heller, G., Krämer, E., Wagner, C., Breitsamter, C. (eds.) New Results in Numerical and Experimental Fluid Mechanics X. Notes on Numerical Fluid Mechanics and Multidisciplinary Design, vol. 132, pp. 801–809. Springer, Cham (2016). https://doi.org/10.1007/978-3-319-27279-5_70
5. May, S., Karl, S., Božić, O.: Development of an eddy dissipation model for the use in numerical hybrid rocket engine combustion simulation. In: 7th European Conference for Aeronautics and Space Sciences, Milano, Italy (2017). https://doi.org/10.13009/EUCASS2017-157
6. Dabanović, A., Martin, J., May, S., Wartemann, V.: Numerical study on post-combustion chamber impact on hybrid rocket performance. In: 3rd International Conference on High-Speed Vehicle Science Technology, Busan, Korea (2024). https://doi.org/10.21203/rs.3.rs-4490644/v1
7. Dabanović, A., Wartemann, V.: Numerical analysis of turbulator plate effects in hybrid rocket combustion. In: 3rd International Conference on Flight Vehicles, Aerothermodynamics and Re-entry (FAR), Arcachon, France (2025)
8. Glaser, C., Hijlkema, J., Anthoine, J.: Bridging the technology gap: strategies for hybrid rocket engines. Aerospace **10**(10), 901 (2023). https://doi.org/10.3390/aerospace10100901
9. Zeriadtke, J.E., Martin, J., Dabanović, A., Wartemann, V.: Hybrid rocket nozzle geometry modelling using level set method. In: 3rd International Conference on Flight Vehicles, Aerothermodynamics and Re-entry (FAR), Arcachon, France (2025)
10. Narsai, P., Momanyi, E., Venkataraman, K., Evans, B.J., Cantwell, B.J.: Indirect heat flux measurements at the nozzle throat of a hybrid rocket motor. In: 51st AIAA/SAE/ASEE Joint Propulsion Conference. American Institute of Aeronautics and Astronautics, Orlando, FL (2015). https://doi.org/10.2514/6.2015-4132
11. Kamps, L., Hirai, S., Sakurai, K., Viscor, T., Saito, Y., Guan, R., Isochi, H., Adachi, N., Itoh, M., Nagata, H.: Investigation of graphite nozzle erosion in hybrid rockets using oxygen/high-density polyethylene. J. Propuls. Power **36**(3), 423–434 (2020). https://doi.org/10.2514/1.b37568
12. Bianchi, D., Nasuti, F.: Numerical analysis of nozzle material thermochemical erosion in hybrid rocket engines. J. Propuls. Power **29**(3), 547–558 (2013). https://doi.org/10.2514/1.b34813
13. Zhao, S., Tian, H., Wang, P., Yu, N., Cai, G.: Steady-state coupled analysis of flowfields and thermochemical erosion of C/C nozzles in hybrid rocket motors. Sci. China Technol. Sci. **58**(3), 574–586 (2015). https://doi.org/10.1007/s11431-015-5775-6
14. Tian, H., Yu, R., Li, C., Zhao, S., Zhu, H.: Numerical and experimental study of the thermochemical erosion of a graphite nozzle in a hybrid rocket motor with a star grain. Acta Astronaut. **155**, 10–22 (2019). https://doi.org/10.1016/j.actaastro.2018.11.007
15. Tian, H., He, L., Yu, R., Zhao, S., Wang, P., Cai, G., Zhang, Y.: Transient investigation of nozzle erosion in a long-time working hybrid rocket motor. Aerosp. Sci. Technol. **118**, 106978 (2021). https://doi.org/10.1016/j.ast.2021.106978
16. Zhang, X., Wang, Z., Wang, R., Lu, C., Yu, R., Tian, H.: Numerical simulation of chemical ablation and mechanical erosion in hybrid rocket nozzle. Acta Astronaut. **192**, 82–96 (2022). https://doi.org/10.1016/j.actaastro.2021.12.012
17. Rotondi, M., Migliorino, M.T., Bianchi, D., Kamps, L., Nagata, H.: Computational analysis and regression laws for nozzle erosion prediction in hybrid rockets. J. Propuls. Power **40**(3), 439–459 (2024). https://doi.org/10.2514/1.B39322
18. Cross, P.G., Boyd, I.D.: Conjugate analyses of ablation in rocket nozzles. J. Spacecr. Rockets **56**(5), 1593–1610 (2019). https://doi.org/10.2514/1.A34311
19. Cross, P.G.: Coupled simulations of finite-rate ablation with pyrolysis in rocket nozzles. J. Thermophys. Heat Transf. **34**(2), 381–392 (2020). https://doi.org/10.2514/1.T5860
20. Hao, X., Yan, Y., Cao, T., Li, W., Zhang, H.: Numerical prediction of the two-phase flow and radiation effects on the thermal environment and ablation of solid rocket nozzle. Int. J. Therm. Sci. **197**, 108794 (2024). https://doi.org/10.1016/j.ijthermalsci.2023.108794
21. Hötte, F., Haupt, M.C.: Transient 3D conjugate heat transfer simulation of a rectangular GOX-GCH4 rocket combustion chamber and validation. Aerosp. Sci. Technol. **105**, 106043 (2020). https://doi.org/10.1016/j.ast.2020.106043
22. Shin, J., Roh, T.-S., Lee, H.J.: Comparison of the semi-empirical heat transfer coefficient for a liquid rocket nozzle with regenerative cooling jacket. J. Propuls. Energy **3**(1), 51–60 (2022). https://doi.org/10.6108/JPNE.2022.3.1.051
23. Betti, B.: Flow field and heat transfer analysis of oxygen/methane liquid rocket engine thrust chambers. Ph.D. thesis, Università degli Studi di Roma "La Sapienza", Roma, Italia (2012)
24. Potier, L., Duchaine, F., Cuenot, B., Saucereau, D., Pichillou, J.: Prediction of wall heat fluxes in a rocket engine with conjugate heat transfer based on large-eddy simulation. Entropy **24**(2), 256 (2022). https://doi.org/10.3390/e24020256
25. Concio, P., Tindaro Migliorino, M., Bianchi, D., Nasuti, F.: Numerical estimation of nozzle throat heat flux in oxygen-methane rocket engines. J. Propuls. Power **39**(1), 71–83 (2023). https://doi.org/10.2514/1.B38811

26. Riedel, N.M., Martin, J., Ohndorf, A., Mundt, C.: Multi-phase injection through bypass: a novel catalytic chamber design. In: 75th International Astronautical Congress (IAC), Milano, Italien (2024)
27. Martin, J., Zeriadtke, J.E., Wartemann, V., Riedel, N.M.: Preliminary design of a throttleable hybrid rocket engine using multiple oxidizer injections. In: 3rd International Conference on Flight Vehicles, Aerothermodynamics and Re-entry (FAR), Arcachon, France (2025)
28. Bartz, D.R.: A simple equation for rapid estimation of rocket nozzle convective heat transfer coefficients. J. Jet Propuls. **27**(1), 49–53 (1957). https://doi.org/10.2514/8.12572
29. Bartz, D.R.: Turbulent boundary-layer flow of rocket heat transfer combustion from rapidly gases and of heated accelerating air. Contractor Report (CR) NASA-CR-62615, Jet Propulsion Lab., California Inst. of Tech., Pasadena, CA, United States (December 1963)
30. Gordon, S., McBride, B.J.: Computer program for calculation of complex chemical equilibrium compositions and applications. Part 1: analysis. Technical report NASA-RP-1311 (1994)
31. Gordon, S., McBride, B.J.: Computer program for calculation of complex chemical equilibrium compositions and applications II. Users manual and program description. Technical report NASA-RP-1311 (1996)
32. Taylor, C.: RocketCEA (2024). https://github.com/sonofeft/RocketCEA. Accessed 15 Apr 2026
33. Poppe, G., Bozic, O., May, S., Bierwagen, N.M.: Characterization of regression rate and combustion process in a high-pressure 2D hybrid rocket engine with optical access. In: Proceedings of the International Astronautical Congress, IAC (2018)
34. Baehr, H.D., Stephan, K.: Wärme- und Stoffübertragung, 6th edn. Springer, Berlin (2008). https://doi.org/10.1007/978-3-540-87689-2
35. WAGNER, B., JACK, S., GENIN, C.: Rocket propulsion in TAU: an overview of the DLR ProTAU project, 12 (2017). https://doi.org/10.13009/EUCASS2017-42
36. Fechter, S., Karl, S., Hannemann, V., Hannemann, K.: Simulation of LOx/GH2 single coaxial injector at high pressure conditions. In: 53rd AIAA/SAE/ASEE Joint Propulsion Conference. American Institute of Aeronautics and Astronautics, Atlanta, GA (2017). https://doi.org/10.2514/6.2017-4765
37. Ivancic, B., Riedmann, H., Frey, M., Knab, O., Karl, S., Hannemann, K.: Investigation of different modeling approaches for computational fluid dynamics simulation of high-pressure rocket combustors. In: Calabro, M., DeLuca, L., Frolov, S., Galfetti, L., Haidn, O. (eds.) Progress in Propulsion Physics, pp. 95–116. EDP Sciences, Munich, Germany (2016). https://doi.org/10.1051/eucass/201608095
38. Allmaras, S.R., Johnson, F.T., Spalart, P.R.: Modifications and clarifications for the implementation of the Spalart–Allmaras turbulence model. In: Computational Fluid Dynamics, Big Island, Hawaii (2012)
39. Westbrook, C.K., Dryer, F.L.: Simplified reaction mechanisms for the oxidation of hydrocarbon fuels in flames. Combust. Sci. Technol. **27**(1–2), 31–43 (1981). https://doi.org/10.1080/00102208108946970
40. Farhat, C., Lesoinne, M.: Two efficient staggered algorithms for the serial and parallel solution of three-dimensional nonlinear transient aeroelastic problems. Comput. Methods Appl. Mech. Eng. **182**(3–4), 499–515 (2000). https://doi.org/10.1016/S0045-7825(99)00206-6
41. Huismann, I., Reimer, L., Strobl, S., Eichstädt, J., Tschüter, R., Rempke, A., Einarsson, G.: Accelerating the FlowSimulator: profiling and scalability analysis of an industrial-grade CFD-CSM toolchain. In: 9th International Conference on Computational Methods for Coupled Problems in Science and Engineering. CIMNE, virtual event (2021). https://doi.org/10.23967/coupled.2021.008
42. Reimer, L., Heinrich, R., Ritter, M., Krumbein, A., Geisbauer, S., Goertz, S., Leicht, T.: Virtual aircraft technology integration platform: ingredients for multidisciplinary simulation and virtual flight testing. In: Scitech 2021 Forum. American Institute of Aeronautics and Astronautics, virtual event (2021). https://doi.org/10.2514/6.2021-1202
43. Kaszynski, A., Derrick, J., German, natter1, Kaszynski, A., FredAns, jleonatti, simonmarwitz, 1081, Correia, D., Addy, D., JackGuyver, jazztekk, jkbgbr, spectereye: Pyansys/Pymapdl: V0.60.3. Zenodo (2021). https://doi.org/10.5281/zenodo.5726008
44. Franze, M., Wartemann, V., Merrem, C.H.-J., Elsässer, H., Ruhe, T., Eggers, T., Weihs, H.: Aerothermal loads analysis of ReFEx by coupled CFD calculations. In: HiSST: 3rd International Conference on High-Speed Vehicle Science And Technology. CEAS, Busan, Korea (2024)
45. Barz, F., Franze, M.: Comparison of different fidelity approaches for the coupled aerothermodynamic heating of hypersonic reentry vehicles. In: HiSST: 3rd International Conference on High-Speed Vehicle Science And Technology. CEAS, Busan, Korea (2024)
46. Franze, M., Barz, F.: Comparison of models for aerothermal load prediction using coupled trajectory simulations of a high lift reentry vehicle. In: HiSST: 3rd International Conference on High-Speed Vehicle Science And Technology. CEAS, Busan, Korea (2024)
47. Reimann, B., Franze, M., Jack, S., Barz, F.: Coupled fluid–structure simulations of panel flutter at high speed. In: AIAA SciTech 2026 Forum, Orlando, USA (2026)
48. Jack, S., Oschwald, M., Eggers, T.: Mechanisms contributing to the dynamic stability of a flexible subscale rocket nozzle. J. Propuls. Power **40**(1), 14–24 (2024). https://doi.org/10.2514/1.B39178
49. Jack, S., Stark, R.: Design and preliminary numerical analysis of a flexible structure for a cold gas nozzle experiment. In: 2nd International Conference on Flight Vehicles, Aerothermodynamics and Re-entry Missions and Engineering, Heilbronn, Germany (2022)
50. Roache, P.J.: Perspective: a method for uniform reporting of grid refinement studies. J. Fluids Eng. **116**(3), 405–413 (1994). https://doi.org/10.1115/1.2910291
51. Roache, P.J.: Quantification of uncertainty in computational fluid dynamics. Annu. Rev. Fluid Mech. **29**(1), 123–160 (1997). https://doi.org/10.1146/annurev.fluid.29.1.123
52. Dakwell, H.M., Badham, H.: Shock formation in conical nozzles. AIAA J. **1**(8), 1932–1934 (1963). https://doi.org/10.2514/3.1965
53. Wartemann, V., Franze, M., Jack, S., Barz, F., Reimann, B.: CoNF2aS^2 - Coupled numerical fluid flight mechanics and structure simulation: Fidelity approaches and validation and application examples. CEAS Space Journal (2026). https://doi.org/10.1007/s12567-026-00774-4

Publisher's Note Springer Nature remains neutral with regard to jurisdictional claims in published maps and institutional affiliations.